Naval Research Laboratory
Washington, DC 20375-5320

NRL/7230/MR—2021/2

Karle Fellowship Research Report

ROBERT J. FOSTER

Coastal and Ocean Remote Sensing Branch
Remote Sensing Division

April 26, 2021

REPORT DOCUMENTATION PAGE

Form Approved
OMB No. 0704-0188

1. REPORT DATE *(DD-MM-YYYY)*	**2. REPORT TYPE**	**3. DATES COVERED** *(From - To)*
26-04-2021	NRL Memorandum Report	12/09/2019 – 12/8/2020

4. TITLE AND SUBTITLE

Karle Fellowship Research Report

5a. CONTRACT NUMBER

5b. GRANT NUMBER

5c. PROGRAM ELEMENT NUMBER
NISE

6. AUTHOR(S)

Robert J. Foster

5d. PROJECT NUMBER

5e. TASK NUMBER

5f. WORK UNIT NUMBER
N2W0

7. PERFORMING ORGANIZATION NAME(S) AND ADDRESS(ES)

Naval Research Laboratory
4555 Overlook Avenue, SW
Washington, DC 20375-5320

8. PERFORMING ORGANIZATION REPORT NUMBER

NRL/7230/MR--2021/2

9. SPONSORING / MONITORING AGENCY NAME(S) AND ADDRESS(ES)

Naval Research Laboratory
4555 Overlook Avenue, SW
Washington, DC 20375-5320

10. SPONSOR / MONITOR'S ACRONYM(S)

NRL-NISE

11. SPONSOR / MONITOR'S REPORT NUMBER(S)

12. DISTRIBUTION / AVAILABILITY STATEMENT

DISTRIBUTION STATEMENT A: Approved for public release; distribution is unlimited.

13. SUPPLEMENTARY NOTES

Karle Fellowship

14. ABSTRACT

This document contains a summary of the research conducted by the author as part of the The Jerome and Isabella Karle Distinguished Scholar Fellowship Program. The research period covered is December 9, 2019 through December 8, 2020.

15. SUBJECT TERMS

Polarized radiative transfer
Air-water interface
3D simulation
Fluorescence

16. SECURITY CLASSIFICATION OF:			**17. LIMITATION OF ABSTRACT**	**18. NUMBER OF PAGES**	**19a. NAME OF RESPONSIBLE PERSON**
					Robert J. Foster
a. REPORT	**b. ABSTRACT**	**c. THIS PAGE**	SAR	26	**19b. TELEPHONE NUMBER** *(include area code)*
U	U	U			(202) 767-5270

This page intentionally left blank.

CONTENTS

FIGURES

TABLES

This page intentionally left blank

EXECUTIVE SUMMARY

The 12-month period under which I conducted research as a Karle fellow was challenging, rewarding, and productive. Despite several difficulties, primarily the switch to a mandatory telework posture due to the COVID-19 pandemic, a large body of important research has been achieved. Much of this work builds upon the foundation provided by the National Research Council (NRC) postdoctoral Research Associateship I held at the NRL between July 2017, and December 2019.

Through my own independent research and collaboration with other NRL employees, substantive progress has been made on the following fronts:

1. Polarized Radiative Transfer Theory
    - Refinement of the Coupled Land-Ocean Vector Renderer (CLOVER) 3D polarized radiative transfer code.
2. Naval Applications of the CLOVER Model
    - Simulation of the influence of Snell's window on optical imaging of an above-water target from below the water surface.
    - Toward detection of unexploded underwater munitions using active fluorometric imaging.

Significant progress has also been made on the following topics, many of which were made possible through collaboration with colleagues at City College of the City University of New York (CCNY), and with current NRC post-docs:

- Fully characterizing, calibrating, deploying, and analyzing data from an all-sky hyperangular spectropolarimeter. [1]
- Exploring the limits of Sun and sky glint correction in fixed geometry hyperspectral observations of the sea surface. [2]
- Utilizing hyperspectral polarimetric imagery of the sea surface to retrieve water optical properties from multi-angular polarimetric data. [3]
- Analyzing airborne hyper-angular, multi-spectral polarimetric images for determination of water-leaving radiance. [4]

Although I contributed significantly to these research topics during my Karle fellowship, detailed documentation on these research efforts may be found in the cited articles and is not included in this report.

This page intentionally left blank

KARLE FELLOWSHIP RESEARCH REPORT

1. INTRODUCTION

This report documents the research I conducted and participated in during the period of December 7th, 2019 through December 8th, 2020, under the Jerome and Isabella Karle Distinguished Scholar Fellowship Program. The research documented here spans several related topics, mostly involving polarized radiative transfer theory (development of a 3D polarized radiative transfer model), and the application of said model for specific Naval applications.

2. POLARIZED RADIATIVE TRANSFER THEORY

2.1 Development of the CLOVER 3D Radiative Transfer Code

I started creating the Coupled Land-Ocean Vector Renderer (CLOVER) radiative transfer code as a side project during my NRC post-doc. The driving force behind it's creation was that no other available code was able to handle arbitrarily complex scenes in 3D, including the effects of optical polarization, as well as incorporating the full-spectrum information necessary for calculating inelastic optical effects like fluorescence and Raman scattering. One of the main accomplishments of my Karle Fellowship was the refinement of the code to a point where is has become a uniquely useful tool for remote sensing. Already, it has been used for two projects (described in Chapter 3), and has won funding from the National Aeronautics and Space Administration (NASA) for a third.

CLOVER is a fully 3D, hyperspectral, and polarization capable code. Scenes of interest may be arbitrarily constructed, including 3D objects, a mix of active and passive sources, detectors, and imaging systems. Optically, each object in a scene is described by its 3D shape, the material it consists of, and its interface with adjacent objects (defined using a bi-directional scattering distribution function (BSDF)). For example, simulation of a glass sphere on a table would require a mathematical description of the sphere shape, the scattering and absorptive properties of the glass and table, and a table of BSDFs describing how photons behave at the interface between air $\leftrightarrow$ glass, air $\leftrightarrow$ table, and glass $\leftrightarrow$ table. All wavelength dependent inputs to the code can be supplied as spectra, so that having multiple wavelengths propagate within the system simultaneously is seamless. When properly set up, CLOVER can calculate the full-spectrum radiance and polarization properties in a single run.

The CLOVER model supports two methods of defining the shape of a scene object: constructive solid geometry (CSG) and surface triangulation (ST) (Fig. 1). CSG allows complex shapes to be constructed from simple shape primitives (cubes, spheres, cones, etc.), through use of set operations (union, intersection, difference) and Affine transformations (translation, rotation, scaling, skew). Since each primitive is completely described using simple geometric relationships, the compound shape is also mathematically exact. This exactness is the keystone which enables CLOVER to precisely and accurately model the optics of complex scenes.

Manuscript approved April 22, 2021.

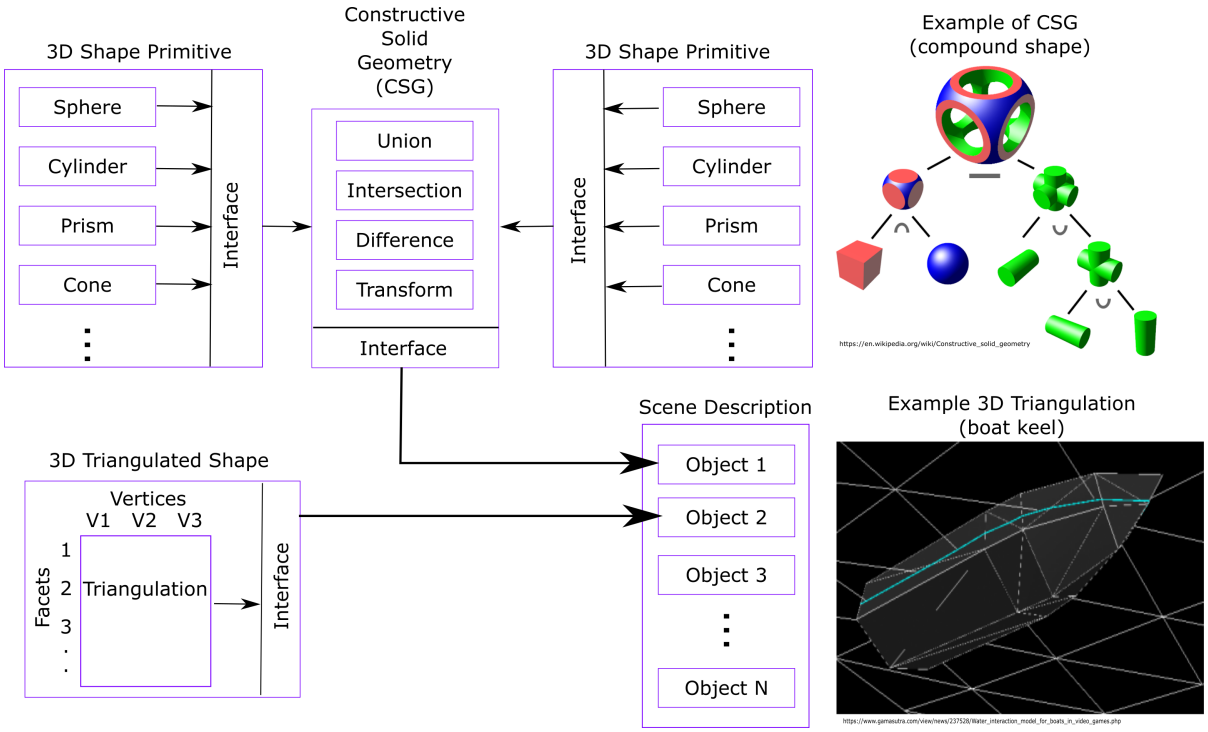

Fig. 1—Scene representation in the CLOVER model. Left: Internal representation of CSG and ST shape models; Top-Right: example of constructive solid geometry shapes; Bottom-Right: Example of a surface triangulation.

Architecturally, CLOVER is written in pure Fortran, conforming to the Fortran-2008 standard. It was written from the ground-up using a modular approach, where new simulation objects and functionality may be seamlessly incorporated into the code without changing the core ray-tracing algorithm. The particular algorithmic constraints for each type of simulation object (spectra, phase matrices, BSDFs, propagation media, shapes, etc.) are defined in an abstract type, where all required inputs and outputs are defined. Tables 1 and 2 provide a partial list of CLOVERs current library of components. Any combination, locations, or permutations of these objects can be used to build arbitrary scenes of interest. New library modules, functionality, and performance-based enhancements are added as time and project constraints allow.

A high-level overview of CLOVERs tracing algorithm is given in Fig. 2. In keeping with the modular nature of the code, each segment of a photon's path is treated separately. After each intersection or scattering event, the photon's state is stored in a queue so that it can be picked up again when it is programatically convenient. If needed, this allows photons in similar states to be processed simultaneously, taking advantage of CPU vector instruction sets and caching.

In order to visualize the scene before committing to a run, CLOVER is able to convert it's internal representation of the scene into OpenSCAD format (https://www.openscad.org/), which can then be previewed with the OpenSCAD software to ensure the scene is correct. Figure 3a is an OpenSCAD rendering of a glass bowl partially filled with water, and Fig. 3b is corresponding radiometric image rendered by CLOVER. From the figure, it's clear that the code is able to account for all 3D effects, including shadowing and refraction by the bowl, internal reflection within the bowl, and specular highlights from the light source. In addition to the

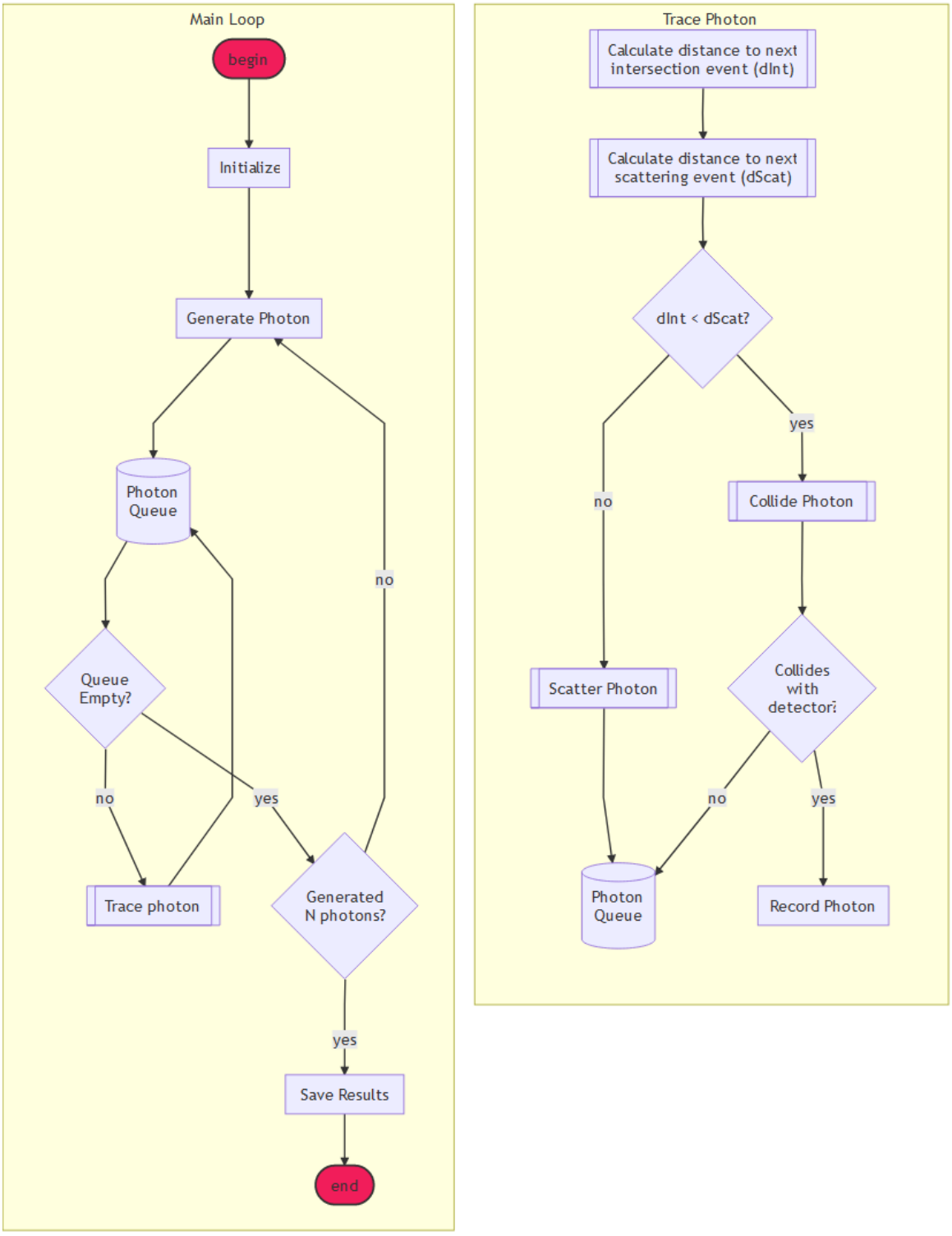

Fig. 2—High-level overview of CLOVERs tracing algorithm.

Shape Primitives	BSDFs	Spectra	Phase Matrices
Sphere	Lambertian	Molecular scattering	Rayleigh
Cuboid	Fresnel	Seawater scattering	Henyey-Greenstein
Cone	Mirror	Molecular depolarization	Two-term Henyey-Greenstein
Cylinder	Identity	Planck's law	Voss-Fry seawater
2D Triangulation	Fluorescing	Pure water absorption	
Circle		Refr. index of N-BK7 glass	
Rectangle		Refr. index of pure water	
CSG node		Refr. index of seawater	
		Refr. index of air	
		Solar irradiance	
		Tabulated spectra	
		Custom spectra	

Table 1—Partial list of CLOVERs current library of shapes, bi-directional scattering distribution functions, spectra, and phase matrices.

Light Sources	Detectors	Propagation Media
Point source	Focal plane	Air with aerosols
Circular source	Circular detector	Seawater with hydrosols
Rectangular source	Angular detector	Schott N-BK7 glass
Sunlight	Camera	Vacuum
	Pinhole camera	
	Spherical detector	

Table 2—Partial list of CLOVERs current library of light sources, detectors, and pre-assembled propagation media.

intensity information, full Stokes polarimetric images of the same scene are simultaneously calculated (not shown).

Other useful features of the program include:

- The ability to produce plots directly using GNUplot (http://www.gnuplot.info), either during a simulation (for progress updates) or to produce plots of output after the simulation is complete.
- Fully integrated error reporting during runtime.
- Ability to draw individual photon paths into the OpenSCAD model for verification of ray tracing behavior.

CLOVER is a long-term investment and will continue to grow and become more capable as project needs change and performance bottlenecks are identified and removed. Some near-term improvements that will be implemented are:

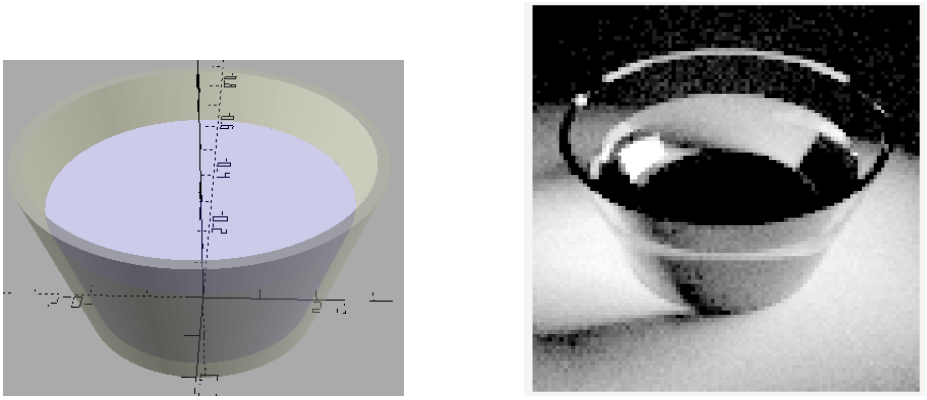

(a) Bowl with water, OpenSCAD (b) Bowl with water, CLOVER

Fig. 3—The OpenSCAD model, and radiance output rendered by CLOVER.

- Parallelizing the code to leverage multi-CPU architectures.
- Additional modules for wind-driven sea surfaces, laser light sources, and passive optical components such as polarizers.
- Improved triangle mesh support
- Additional variance reduction techniques, such as local estimates.

3. NAVAL APPLICATIONS

Despite existing for only a little over a year, CLOVER has already been found to be a useful tool for remote sensing and instrument design. In the following sections, I will describe the work that has been achieved thus far with CLOVER for specific Naval applications.

3.1 Modeling the Effect of Snell's Window on Optical Imaging of Above-Water Targets From Below The Surface

3.1.1 Background

A specific operational Navy need is narrow field-of-view (FOV) imaging through the water/air interface from a submerged position. There have been several technical approaches developed and tested in the past for wide FOV (larger than 40 °) imaging under the surface (e.g. virtual periscope), but they are primarily for situational awareness and have not met the specific operational requirements of narrow FOV (less than 14 ° degrees) image correction. In astronomical imaging, there has been more than fifty years of theoretical and experimental work, some of which was developed at the NRL, in addressing image degradation caused by atmospheric turbulence using wavefront sensing and correction techniques. This project aimed to apply this astronomical imaging expertise to state-of-the-art, image-intensified sensors to develop, characterize, and test a breadboard prototype intensified underwater imager that actively corrects for distortions caused by the sea surface. The principal investigator (PI) for this project is Dr. Freddie Santiago.

As part of this work, investigations into theoretical optical distortions due to sea surface refraction were conducted. CLOVER was used to model and predict the baseline distortion that would happen in the ideal case of a calm sea surface. Two selected scenarios are described here. In each one, an array of Lambertian reflecting tiles was created and imaged at different angles through the air-water interface. All simulation results are presented at 440 nm.

3.1.2 Horizontal Target, Upward Imaging

In this first experiment, the goal was to test CLOVERs ability to model refraction by the sea surface and reproduce Snell's window, or the cone of visibility limited by total internal refraction by the interface. The simulation setup is show in Fig. 4. The simulation includes an 8×8 checkerboard pattern of tiles which was positioned directly over a simulated tank of size 3 m $\times$ 3 m $\times$ 1 m. A pinhole camera with a 55 $^\circ$ FOV was positioned at the bottom of the tank, looking upward. The density of the focal plane was set to 150×150 pixels. The water in the tank did not contain any scatterers, since the goal was to analyze distortions caused by the surface.

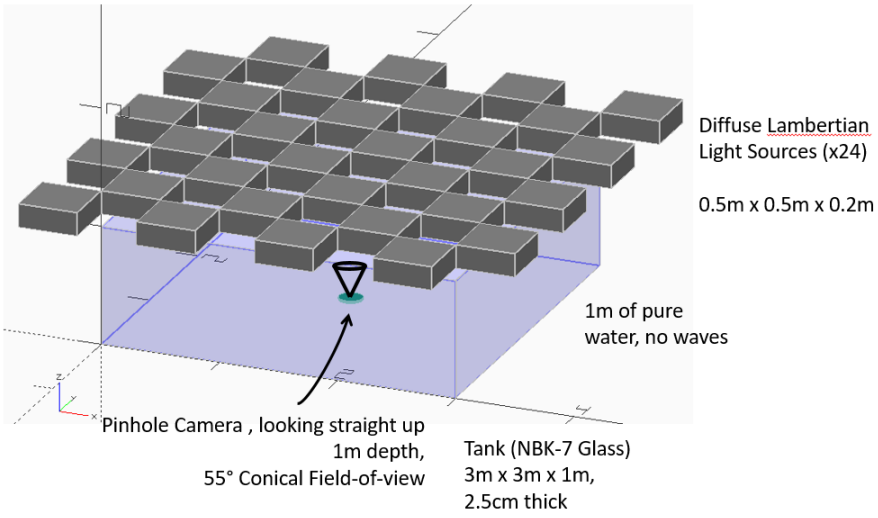

Fig. 4—OpenSCAD representation of the first experiment, to test the modeling of Snell's window.

The simulation results are shown in Fig. 5. The left side of the figure shows the radiance image, in which Snell's window can clearly be seen. The distortion of the grid pattern around the edges of the window are consistent with theory, and indicate that only about a 2-tile diameter is visible without distortions. The edges of the circular FOV show additional grid patterns, which arise due to reflections from within the tank, since the edges of the grid were slightly visible through the sides of the tank. On the right hand side are the polarization parameters. A definition of the various polarization parameters may be found in Appendix A. It can be seen that the degree of linear polarization (DoLP) increases from 0 % in the center of the window out to nearly 10 % as the edge. There is no significant change in the U/I or V/I components in the window itself, but there is significant fluctuations caused by total internal reflections by the underside of the sea surface. In real images, this effect may be a useful indicator for the boundaries of the window, allowing to separate total internal reflected light from transmitted light.

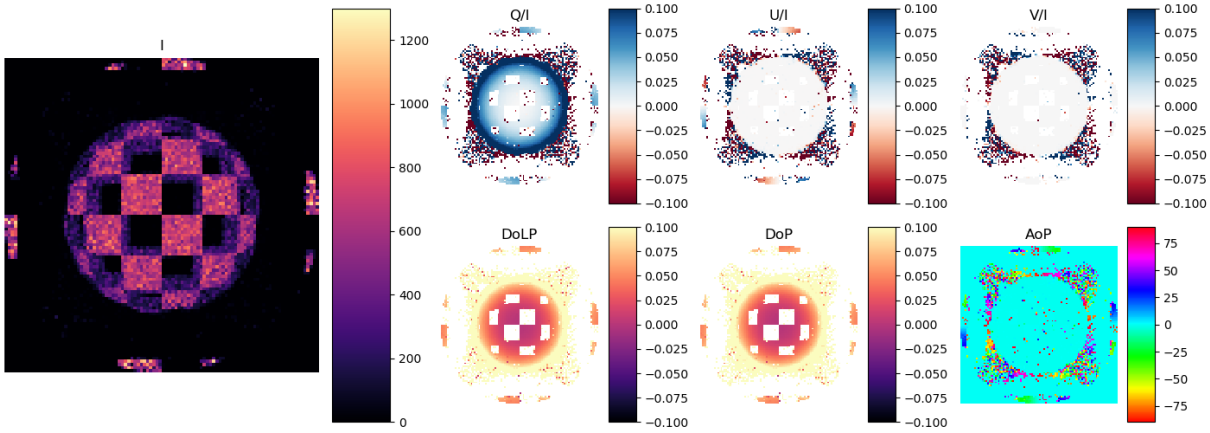

Fig. 5—CLOVERs rendering of the first experiment. The radiance image is shown on the left, and all polarization parameters are shown on the right.

3.1.3 Vertical Target, Upward Viewing

In the first experiment, the coarseness of the tiles did not contain sufficient spatial information to simulate the distortion near the edges of Snell's window. The next experiment was designed to maximize this effect. As can be seen from Figure 6, the density of the grid was increased to a 16 × 16 checkerboard pattern, and oriented vertically such that one edge was just above the surface of the water. This emulates viewing a distant above-water target on the horizon. The pinhole camera FOV was decreased to 5 ° and the focal plane density was increased to 200 × 200 pixels. The camera was aimed directly at the critical angle of total internal reflection to maximize viewing of the distortion.

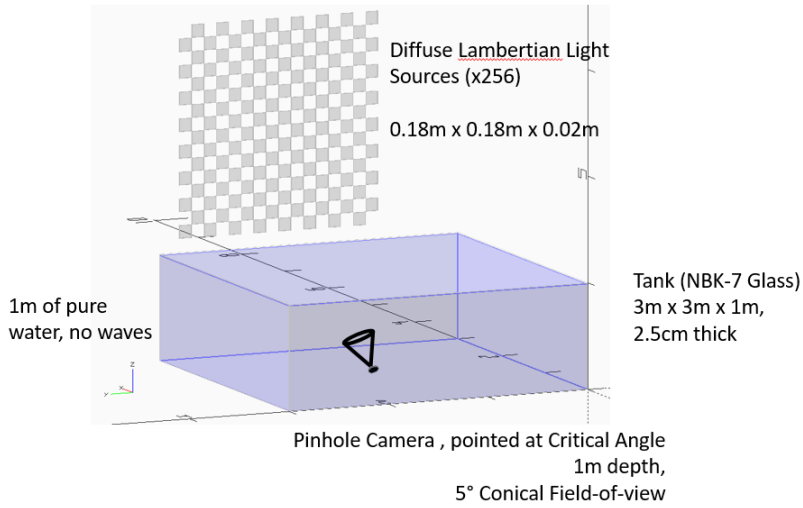

Fig. 6—OpenSCAD representation of the second experiment, to highlight the distortion caused by the edges of Snell's window.

In Figure 7, we can see the corresponding CLOVER output. In the left panel is the radiance image. The circular edge of Snell's window can be clearly seen, and all of the 256 tiles are visible through the distortion, at least to some extent. The very bottom row of tiles suffers from very high distortion, but is still

visible. Interestingly, in the bottom half of the image, a reflection of the array is visible without distortion due to reflection of light coming from the array on the tank walls. This is even more evident in the U Stokes component on the right of the image, where there is a clear shift in the polarization angle of the light across the center of the image. Such a shift would not occur because of transmission through Snell's window [5] (also as evidenced by Figure 5). The Q component again increases with transmission angle through the window. The increase appears less pronounced compared to the prior experiment, but since the FOV is much smaller (5 ° vs. 55 °), the change with angle is not as visible. Since the above surface light is completely unpolarized, any polarization seen within Snell's window is produced by the Fresnel transmission process.

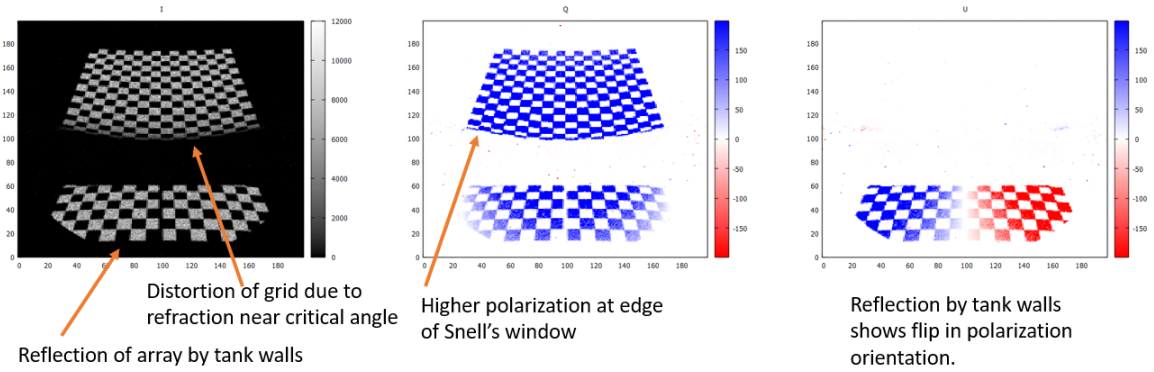

Fig. 7—CLOVERs output for the second experiment. The radiance image is shown on the left, and the Q and U polarization parameters are shown on the right.

In both experiments, CLOVERs output was used to compare and contrast with physical measurements made in a wave tank from several submerged cameras. Images were acquired of a checkerboard pattern printed on a poster-board, and were found to be in excellent agreement with modeled results. This project was a short term demonstration of capability, and a follow-on proposal has been submitted to continue the work, including additional radiative transfer modeling using CLOVER.

To summarize, in this work CLOVER was used to understand the baseline spatial distortion in intensity and polarization that light undergoes when transmitted through a calm sea surface. If this project is continued in some form, CLOVER will be expanded to include realistic wind-driven sea surfaces [6], and further images will be produced to analyze the spatial distortions caused by wave swells.

3.2 Toward Use of Fluoresced Light For The Detection of Unexploded Underwater Munitions

3.2.1 Background

The sponsor for this project is the Department of Defense (DoD) Strategic Environmental Research and Development Program (SERDP) Munitions Response Program Area. The project lead is Dr. Steven Ackleson. This is a proof-of-concept project which aims to test the hypothesis that the active fluorometric imaging (AFI) technique is a viable approach for the classification of benthic features and detection of anthropogenic objects on the seafloor. The ultimate goal is to develop a system capable of detecting unexploded munitions on the seafloor.

Objects which are submerged in a shallow body of water are rapidly colonized by micro-organisms and larger animals, many of which fluoresce in unique ways due to their natural pigments [7]. Dyes, lubricants,

and identifying markings on anthropogenic objects often exhibit fluorescence in a similar manner. Such objects absorb incident radiation at one wavelength, and re-emit it at a longer wavelength. The energy of the re-emitted light is primarily governed by the fluorescence efficiency of the material and the intensity of the incident light, although some other factors also apply for biological fluorescence.

In AFI, a bright light source is used to illuminate a patch of the sea bottom, or object of interest, and the fluoresced light (the inelastic response) is observed with an imaging system. AFI has several advantages over reflectance imaging, where the camera observes the scattering and reflection by the light source (the elastic response). Primarily, the fluoresced light is emitted at a longer wavelength than the excitation light. If the imaging is done at night time (the usual case), the fluoresced light is completely separable from the illumination, and thus very sensitive optics may be used to view it, without regard for interference from the bright source. Secondly, even though the fluoresced light is not as intense, it does not experience as much scattering on the way to the observer since the path length is half as much (assuming that the light source and observer are co-located). Thus, an image formed of the fluoresced light contains no contribution from scattering of the excitation wavelength, and a sharper image (containing significantly less background scatter) may be obtained than otherwise possible. Third, the spectra of this fluoresced light is highly species and material specific, providing a very useful tool for the identification and characterization of the fluorescing material.

3.2.2 Testing the AFI Concept

The first of two experiments that involved CLOVER was a purely theoretical one, where the AFI concept was demonstrated using a 3D simulation.

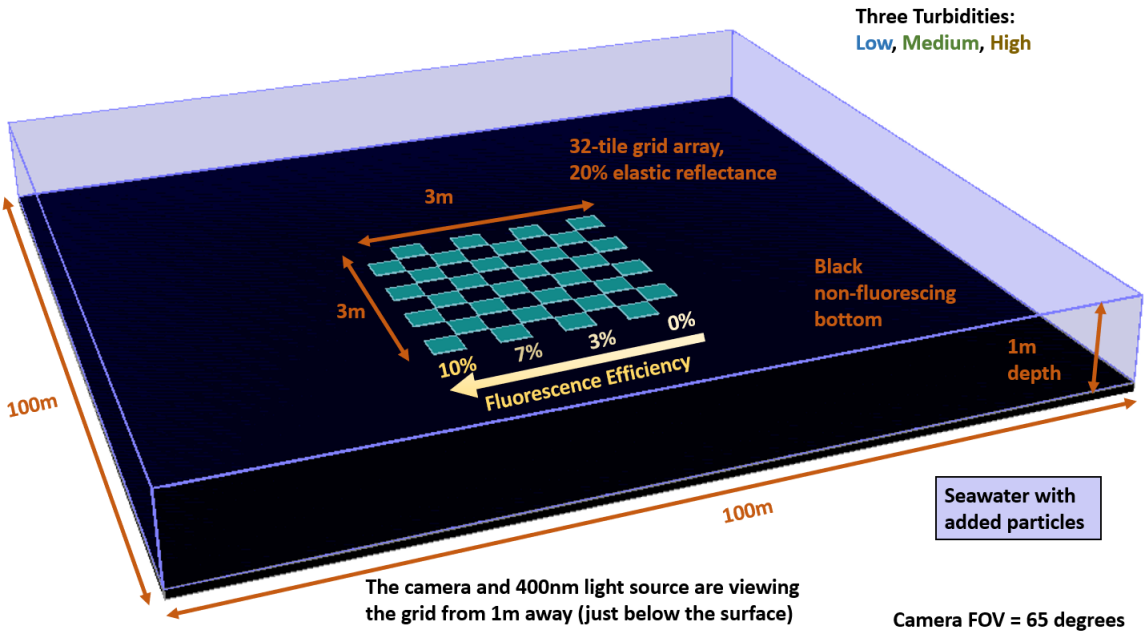

Fig. 8—OpenSCAD representation of submerged fluorescent tiles.

The setup for the first experiment is shown in Fig. 8. The simulation domain was a rectangular cuboid of 100 m width and length, and 1 m deep. The bottom of the domain was completely absorbing (black). An 8 ×

8 array of fluorescing tiles was created at the bottom, arranged in a checkerboard pattern. The whole grid was 3 m square. For the elastic response, each of the tiles was assigned a Lambertian bi-directional reflectance distribution function (BRDF) with an albedo of 20 %. The inelastic response was also Lambertian, but the emission wavelength was chosen using a Gaussian profile with a 40 nm mean shift, and 2 nm standard deviation. This type of response is commonly observed in both organic and synthetic materials [8]. The domain was filled with seawater, with added mineral particles representing scattering by the water body. The fluorescence efficiency was linearly increased from 0 % for the right-most column, to 20 % for the left-most column. The virtual camera is positioned just below the water surface, centered over the grid, and viewing it through 1 m of water. The FOV of the camera is 130 ° (full angle), and the focal plane was 150 pixels square. Three different simulations were performed, each with a different level of mineral concentrations characterized by the scattering coefficient (b). The concentrations are low turbidity (b = 0.3 m^{-1}), moderate turbidity (b = 0.8 m^{-1}), and high turbidity (b = 3.0 m^{-1}).

The resulting simulated images are shown in Fig. 9. Viewing through 1 m of water, the reflectance images (left panels) indicates a progressive increase in backscatter from the intervening water as the pathlength increases with view angle from nadir at the center of the target to 65 ° at the edge. The fluorescence images (right panels) do not suffer from path radiance and are thus sharper compared with the reflectance images. Fluorescence efficiency increases within the grid pattern from right to left and CLOVER clearly captures the resulting increase in contrast in the same direction. Maximum contrast occurs at nadir (image center) where the imaging pathlength is shortest and, therefore, image attenuation is smallest. The fluorescence pattern disappears along the right side of the image where efficiency is zero.

3.2.3 Reproducing Measurement Data Taken with the ECOTONE-UHI Line Scanner

As part of the SERDP project, a underwater hyperspectral imager (UHI) was purchased from ECOTONE (Scientific UHI-2000) (https://ecotone.com/). A major goal of the project was to assess the suitability of the instrument for use with the AFI concept in a laboratory setting. In order to do this, three fluorescence targets were set up on a rotating drum inside of a 1 × 1 × 3 m tank. The UHI and a high power 464 nm light emitting diode (LED) dive lamp were set up outside the tank. The imaging distance to the targets was 1 m. The drum was rotated in order to simulate forward movement of the UHI linescanner.

The experiment was repeated with three different water turbidity levels. Particles of Arizona Ultra-fine test dust (average particle diameter of 5 μm) were added in increasing concentrations to emulate increases in turbidity. The optical properties of both the water (measured with a WETLabs ac-9 absorption and scattering meter), and the reflectance/fluorescence targets are listed in Table **??**.

To simulate this scene with CLOVER, the exact measurements and thickness of the tank were considered in order to model the reflection by the tank walls as accurately as possible. Since the ECOTONE is a line scanner, and CLOVER is not yet capable of performing time-dependent simulations, we modeled successive scans (forming an image) by the UHI as a static scene using a pinhole camera model. Some differences between these two modalities exist, mainly that the imaging path-length is larger for a pinhole camera since the scene does not move to bring each successive point closer to the pixel footprint of the scan. This causes some additional scattering to be apparent in the simulated images with increasing viewing angle. Regardless, a 99% elastic reflectance target, and two fluorescence targets (low and high) representing the maximum and minimum of typical natural benthic fluorescence were attached to a round drum, in order to mimic the physical experimental setup as closely as possible. The fluorescence efficiency for each target was measured with the UHI and used in the simulations. In order to model the low and high targets separately (as opposed

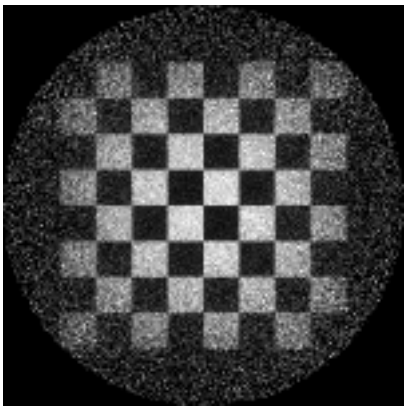

(a) Low turbidity, elastic

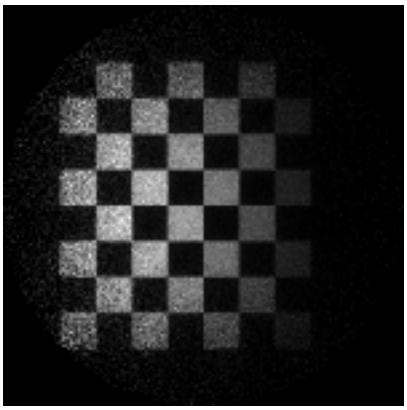

(b) Low turbidity, fluoresced

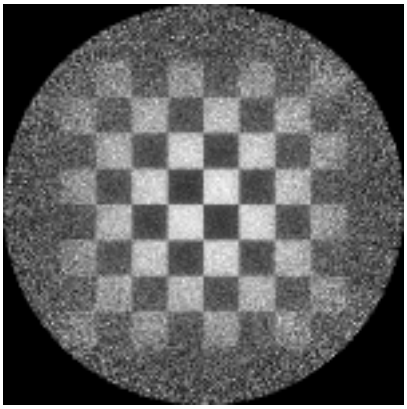

(c) Medium turbidity, elastic

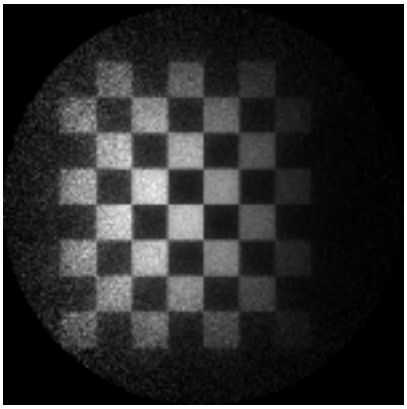

(d) Medium turbidity, fluoresced

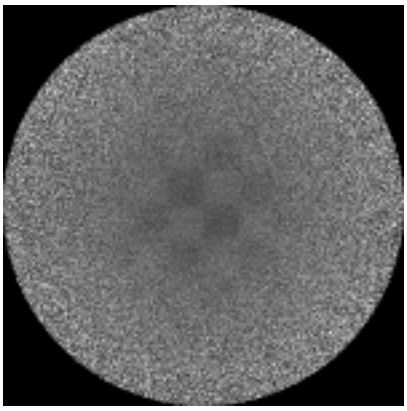

(e) High turbidity, elastic

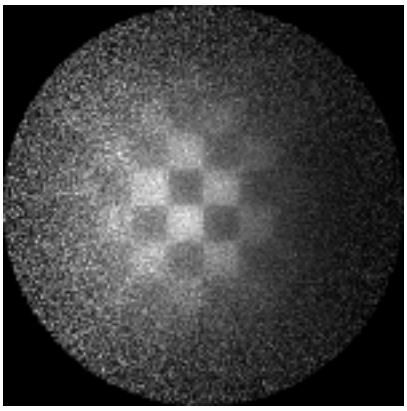

(f) High turbidity, fluoresced

Fig. 9—Simulations of the AFI concept using the CLOVER radiative transfer model. Each image is viewed through 1 m of water, for three different turbidities. The reflectance images are shown in the left panels, and the fluorescence images are on the right. Fluorescence efficiency increases within the grid pattern from right to left, disappearing along the right side of the image where efficiency is zero.

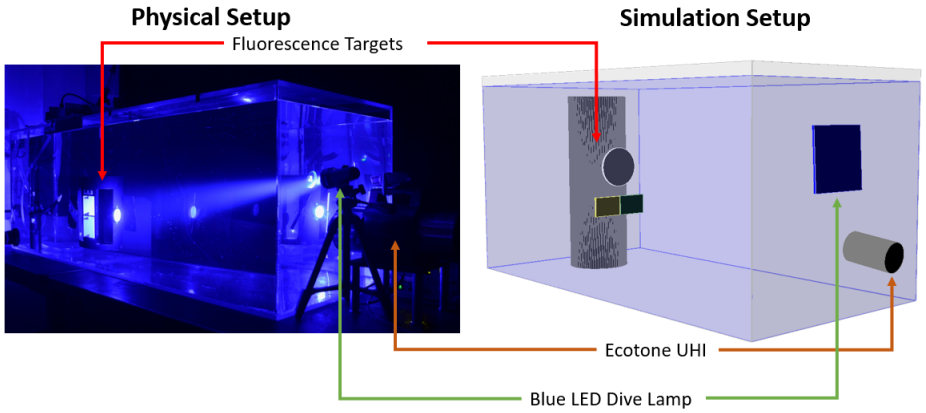

(a) Comparison of physical vs simulated experiment

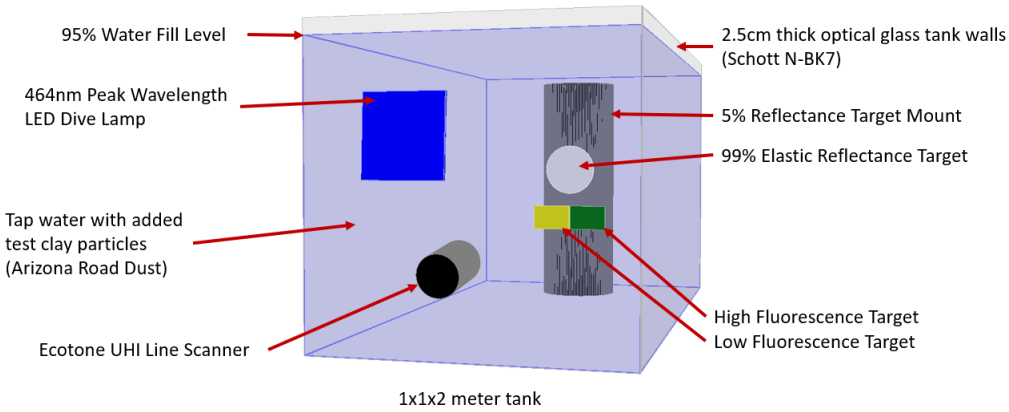

(b) Description of simulated targets

Fig. 10—Scene description for comparison of simulated versus measured fluorescence measurements.

to the real experiment when both target signatures were combined), the fluorescence emission was assumed to be a Gaussian function centered on the peak emission wavelength for each target. A comparison of the physical and simulated setup can be seen in Figure 10.

A series of CLOVER radiance images corresponding to the different wavelength and turbidity levels are shown in Figure 11. The turbidity increases from top to bottom of the page. The imaging wavelengths change from left to right. The elastic signal is on the leftmost column, where all three targets are visible. The middle column is 539 nm, the peak emission wavelength of the low fluorescence target. The rightmost column is 496 nm, the peak emission wavelength of the high fluorescence target. It can clearly be seen that with increasing turbidity, the reflectance target becomes harder and harder to resolve, eventually vanishing from the image entirely for the highest turbidity. Both the low and the high fluorescence targets are still visible, even at the highest turbidity. As mentioned above, the reason for this is because the fluoresced light travels through half the distance that the elastic light does (since it originates at the target), and the fluoresced light is only forward-scattered by the intervening water column. The elastic signal, by contrast, is backscattered by the water column before it even reaches the targets, causing the blurring and scattering visible in the images.

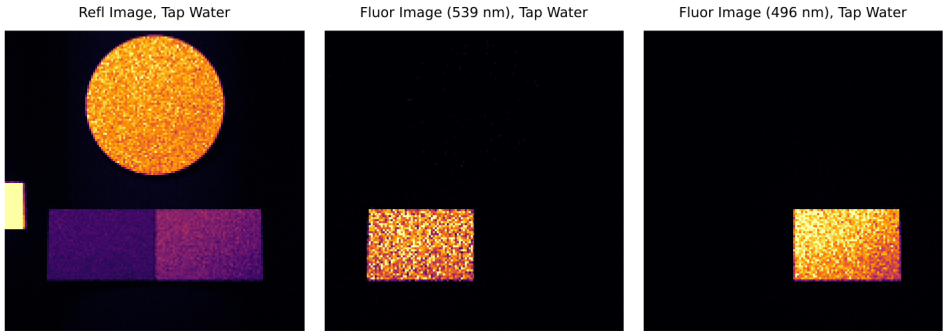

(a) Refl, Tap Water (b) Low Fl, Tap Water (c) High Fl, Tap Water

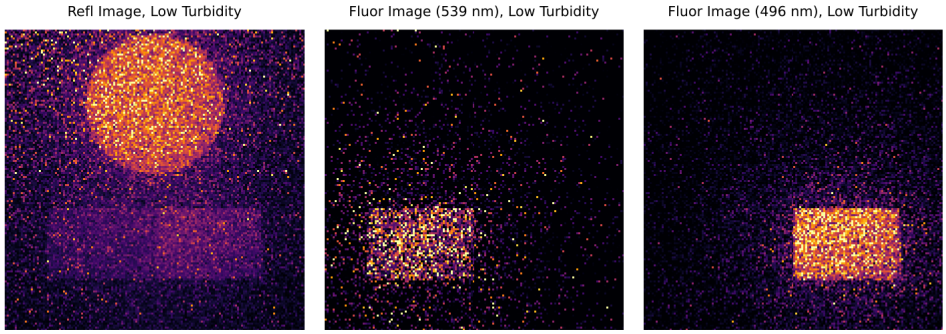

(d) Refl, Low Turbidity (e) Low Fl, Low Turbidity (f) High Fl, Low Turbidity

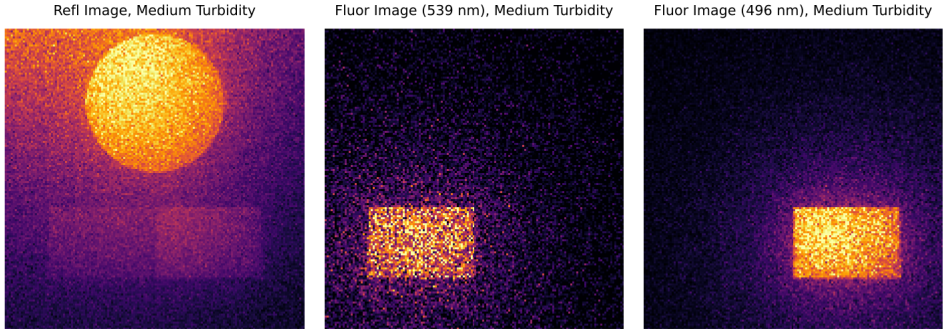

(g) Refl, Med Turbidity (h) Low Fl, Med Turbidity (i) High Fl, Med Turbidity

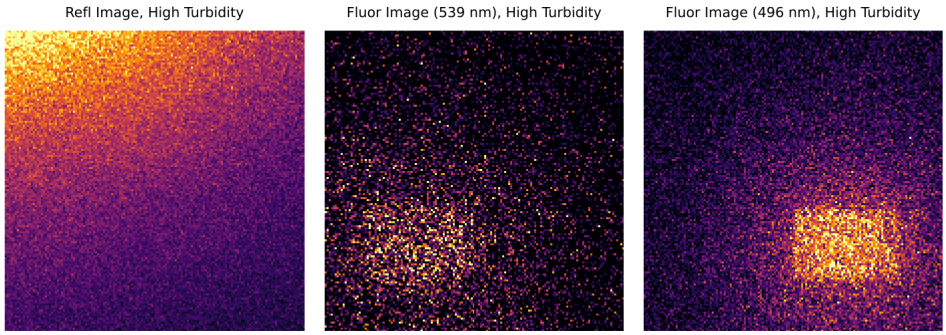

(j) Refl, High Turbidity (k) Low Fl, High Turbidity (l) High Fl, High Turbidity

Fig. 11—Simulated images of elastic and fluorescence targets at four turbidity levels. From top to bottom: Tap water, low, medium, and high turbidity. From left to right: elastic, low Fl target, high Fl target.

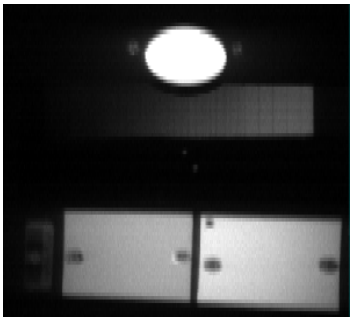

(a) Refl, Tap Water

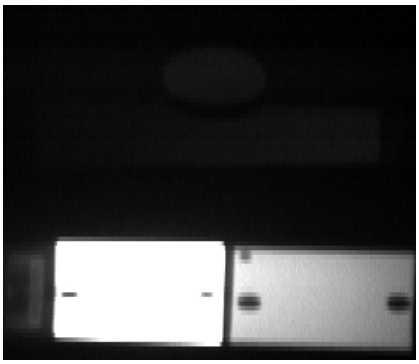

(b) Low Fl, Tap Water

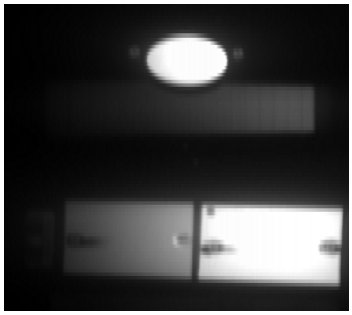

(c) Refl, Low Turbidity

(d) Low Fl, Low Turbidity

(e) Refl, Medium Turbidity

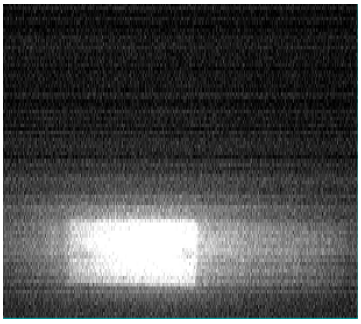

(f) Low Fl, Medium Turbidity

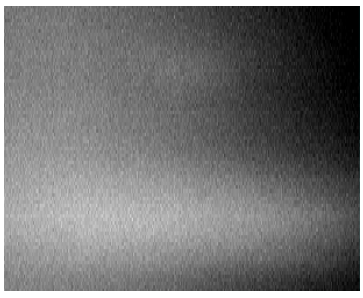

(g) Refl, High Turbidity

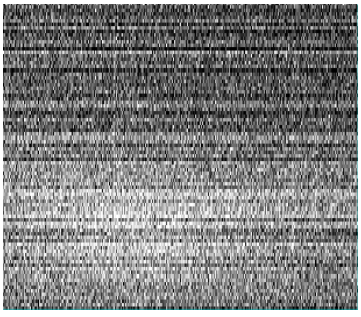

(h) Low Fl, High Turbidity

Fig. 12—Images acquired with the ECOTONE UHI linescanner, for elastic and fluorescence targets at four turbidity levels. From top to bottom: Tap water, low, medium, and high turbidity. From left to right: elastic wavelength (464 nm), low Fl peak (539 nm).

	Tap Water	Low Turbidity	Medium Turbidity	High Turbidity
Attenuation (464 nm) m^{-1}	0.22	2.71	3.78	6.25
Attenuation (496 nm) m^{-1}	0.19	2.67	3.73	6.18
Attenuation (539 nm) m^{-1}	0.18	2.62	3.66	6.07
Elastic Target albedo (646 nm)	99%	99%	99%	99%
FT_{low} albedo (646 nm).	27%	27%	27%	27%
FT_{low} Fl Eff (539 nm).	0.4%	0.4%	0.4%	0.4%
FT_{high} albedo (646 nm)	57%	57%	57%	57%
FT_{high} Fl Eff (496 nm)	4.7%	4.7%	4.7%	4.7%

Table 3—Target and Water Parameters

The corresponding measured images are shown in Figure 12. Similar to Figure 11, water turbidity increases from top to bottom. The elastic wavelength from the linescanner is shown in the leftmost column, and images at the peak emission wavelength for the low fluorescence target are shown in the right-hand column. Images for the high fluorescence target were not available at the time of writing. In all cases, the measurement data is perfectly reproduced by the model. The reflectance targets are still visible, although very blurred up through the medium turbidity level, but again completely vanish for the highest turbidity. In agreement with the simulated results, the low fluorescence target is still slightly visible despite the significant presence of sensor noise and fluctuating gain parameters in each scan. The high fluorescence images are expected to similarly mirror the simulated results.

In summary, CLOVER was successfully able to reproduce experimental measurements for a range of turbidity levels for both elastic and fluorescing targets, including the full replication of the physical experiment. This successful closure has validated both CLOVER and the AFI concept, and funding for additional work expanding on these results has been submitted.

ACKNOWLEDGMENTS

The author would like to thank several people for their support, assistance, and willingness to include me in their research: Jeffrey Bowles (NRL), Alex Gilerson (CCNY), Ahmed El-Habashi (NRC), Deric Gray (NRL), Freddie Santiago (NRL), Steve Ackleson (NRL), and Philipp Grötsch (formerly CCNY, now Flying Gybe, Inc.).

REFERENCES

1. R. Foster, D. Gray, J. Bowles, D. Korwan, I. Slutsker, M. Sorokin, M. Roche, A. Smith, and L. Pezzaniti, "Mantis: an all-sky visible-to-near-infrared hyper-angular spectropolarimeter," *Applied Optics* **59**(20), 5896–5909 (2020), doi:10.1364/AO.393822. URL `https://doi.org/10.1364/AO.393822`.

2. P. M. M. Groetsch, R. Foster, and A. Gilerson, "Exploring the limits for sky and sun glint correction of hyperspectral above-surface reflectance observations," *Applied Optics* **59**(9), 2942–2954 (2020), doi:10.1364/AO.385853. URL `https://doi.org/10.1364/AO.385853`.

3. A. Gilerson, C. Carrizo, A. Ibrahim, R. Foster, T. Harmel, A. El-Habashi, Z. Lee, X. Yu, S. Ladner, and M. Ondrusek, "Hyperspectral polarimetric imaging of the water surface and retrieval of water optical parameters from multi-angular polarimetric data," *Applied Optics* **59**(10), C8–C20 (2020), doi:10.1364/AO.59.0000C8. URL https://doi.org/10.1364/AO.59.0000C8.

4. A. El-Habashi, J. Bowles, R. Foster, D. Gray, and M. Chami, "Polarized observations for advanced atmosphere-ocean algorithms using airborne multi-spectral hyper-angular polarimetric imager," *Journal of Quantitative Spectroscopy and Radiative Transfer* **262**, 107515 (2021), ISSN 0022-4073, doi:10.1016/j.jqsrt.2021.107515. URL https://doi.org/10.1016/j.jqsrt.2021.107515.

5. R. Foster and A. Gilerson, "Polarized Transfer Functions of the Ocean Surface for Above-Surface Determination of the Vector Submarine Light Field," *Applied Optics* **55**(33), 9476–9494 (2016), doi:10.1364/AO.55.009476. URL https://doi.org/10.1364/AO.55.009476.

6. C. D. Mobley, "Polarized Reflectance and Transmittance Properties of Wind-blown Sea Surfaces," *Applied Optics* **54**(15), 4828–4849 (2015), doi:10.1364/AO.54.004828. URL http://dx.doi.org/10.1364/AO.54.004828.

7. C. H. Mazel, M. P. Strand, M. P. Lesser, M. P. Crosby, B. Coles, and A. J. Nevis, "High-resolution determination of coral reef bottom cover from multispectral fluorescence laser line scan imagery," *Limnology and Oceanography* **48**(1part2), 522–534 (2003), ISSN 0024-3590, doi:10.4319/lo.2003.48.1_part_2.0522. URL https://doi.org/10.4319/lo.2003.48.1_part_2.0522.

8. M. Tzortziou, P. J. Neale, C. L. Osburn, J. P. Megonigal, N. Maie, and R. JaffÉ, "Tidal marshes as a source of optically and chemically distinctive colored dissolved organic matter in the Chesapeake Bay," *Limnology and Oceanography* **53**(1), 148–159 (2008), ISSN 1939-5590, doi:10.4319/lo.2008.53.1.0148. URL http://dx.doi.org/10.4319/lo.2008.53.1.0148.

9. H. C. v. d. Hulst, *Light scattering by small particles* (John Wiley and Sons, Inc, New York, 1957), ISBN 0-486-64228-3. URL https://books.google.com/books?id=777DAgAAQBAJ.

10. M. I. Mishchenko, *Electromagnetic Scattering by Particles and Particle Groups: An Introduction* (Cambridge University Press, Cambridge, 2014), ISBN 1139867121.

11. R. D. M. Garcia, "Fresnel boundary and interface conditions for polarized radiative transfer in a multilayer medium," *Journal of Quantitative Spectroscopy and Radiative Transfer* **113**(4), 306–317 (2012), ISSN 0022-4073, doi:10.1016/j.jqsrt.2011.11.015. URL http://dx.doi.org/10.1016/j.jqsrt.2011.11.015.

12. P. W. Zhai, G. W. Kattawar, and Y. Hu, "Comment on the transmission matrix for a dielectric interface," *Journal of Quantitative Spectroscopy and Radiative Transfer* **113**(16), 1981–1984 (2012), ISSN 0022-4073, doi:10.1016/j.jqsrt.2012.07.001. URL http://www.sciencedirect.com/science/article/pii/S0022407312003263.

13. R. D. M. Garcia, "Response to "Comment on the transmission matrix for a dielectric interface"," *Journal of Quantitative Spectroscopy and Radiative Transfer* **113**(17), 2251–2254 (2012), ISSN 0022-4073, doi:10.1016/j.jqsrt.2012.08.008. URL http://dx.doi.org/10.1016/j.jqsrt.2012.08.008.

ACRONYMS

AFI active fluorometric imaging. 8–11, 15, E-1
AoP angle of polarization. 20
BRDF bi-directional reflectance distribution function. 10
BSDF bi-directional scattering distribution function. 1, 2, 4
CCNY The City College of the City University of New York. 15, E-1
CLOVER Coupled Land-Ocean Vector Renderer. iv, 1–12, 15, 19, E-1
CSG constructive solid geometry. 1, 2, 4
DoD Department of Defense. 8
DoLP degree of linear polarization. 6, 20
FOV Field-of-view (full angle). 5–8, 10
LED light emitting diode. 10
NASA National Aeronautics and Space Administration. 1
NRC National Research Council. 1, 15, E-1
PI principal investigator. 5
SERDP Strategic Environmental Research and Development Program. 8, 10
ST surface triangulation. 1, 2
UHI underwater hyperspectral imager. 10, 14

This page intentionally left blank

Appendix A

DESCRIPTION OF POLARIZED LIGHT

The electric field of a time-harmonic plane wave propagating in an infinite, non-absorbing, homogeneous space may be described by the equations: [9]

$$\begin{aligned} E_l(t) &= a_l e^{-\jmath\varepsilon_1} e^{-\jmath kz+\jmath\omega t} \\ E_r(t) &= a_r e^{-\jmath\varepsilon_2} e^{-\jmath kz+\jmath\omega t} \end{aligned} \tag{A1}$$

where z is the direction of wave propagation, a_l and a_r are the electric field amplitudes parallel and perpendicular to the local meridian plane, k is the wave number, ω is the angular frequency, ε_1 and ε_2 are the phase angles, and $\jmath$ is $\sqrt{-1}$.

Through quadratic combinations of the l and r components, we can define a time-averaged, real-valued matrix called a Stokes vector which is able to describe the complete state of polarization: [9, 10]

$$\boldsymbol{S} = \begin{bmatrix} I \\ Q \\ U \\ V \end{bmatrix} = \frac{1}{2}\sqrt{\frac{\epsilon_r}{\mu_r}} \begin{bmatrix} E_l E_l^* + E_r E_r^* \\ E_l E_l^* - E_r E_r^* \\ E_l E_r^* + E_r E_l^* \\ \jmath(E_l E_r^* - E_r E_l^*) \end{bmatrix} \tag{A2}$$

where ϵ_r and μ_r are the relative electric permittivity and relative magnetic permeability of the propagation medium. It is important to note that the $\boldsymbol{S}$ defined in equation A2 (and used throughout this report) is a *diffuse* Stokes vector with units of radiance, as opposed to a *coherent* Stokes vector describing a plane wave of light propagating in exactly one direction, with units of irradiance. The difference is important when describing the transmission of diffuse polarized light through a dielectric interface such as the walls of a tank [11–A13] in Section 3. Although CLOVER uses coherent Stokes vectors for it's internal calculations, the diffuse Stokes vector is the final output.

The I component describes the total radiance, Q describes the tendency of the electric field to oscillate in the parallel or perpendicular direction with respect to the local meridian plane, and U describes the tendency for oscillation in the $\pm 45^\circ$ directions. V denotes left handed or right handed circular polarization, but is usually negligible when considering natural light sources and environments. Some V component is present is the described work, which is induced by total internal reflection by the water and tank.

Additionally, since natural light sources are polychromatic, all Stokes vectors are constrained by the Stokes-Verdet inequality: [10]

$$\bar{I}^2 \geq \bar{Q}^2 + \bar{U}^2 + \bar{V}^2 \tag{A3}$$

and the bars indicate time-averaged polychromatic Stokes components.

We can also define the DoLP and angle of polarization (AoP), which describes the percentage of linearly polarized light present, and the orientation angle of such light with respect to the local meridian:

$$DoLP = \frac{\sqrt{Q^2 + U^2}}{I} \tag{A4}$$

$$AoP = \frac{1}{2} \tan^{-1} \left(\frac{U}{Q} \right) \tag{A5}$$